Analysis of Rate-Limiting Factors in Thick Electrodes for Electric Vehicle Applications

Byoung-Sun Lee, Zhaohui Wu, Victoria Petrova,* Xing Xing, Hee-Dae Lim, Haodong Liu, and Ping Liu ⓞ**,z

Electrochemical Material Science Laboratory, Department of Nanoengineering, University of California, San Diego, La Jolla, California 92093, USA

Increasing electrode thickness and loading can help Li-ion batteries achieve higher energy densities, but the resulting decay in electrochemical performance at elevated rates remains a significant challenge. In order to design an optimal thick electrode, understanding how performance loss occurs is necessary. While it is known that both ionic and electronic conductivity contribute to rate performance, we observed a stronger correlation between electronic conductivity and electrochemical performance of electrodes at a loading of >25 mg/cm^2 under C/3 to 1C, rates most relevant to electric vehicle applications. To illustrate this effect, we explore the mud-cracking phenomenon during electrode fabrication to obtain narrow, vertical channels which reduce electrode tortuosity, and therefore decrease the liquid phase ionic resistance in thick electrodes. Variation in crack densities enables us to systematically investigate the effects of ionic and electronic conductivity on electrochemical performance in electrodes with identical overall porosity and composition. Rate and cycling performances of mud-cracked thick electrodes have stronger correlations with electronic conductivity than ionic conductivity. These findings shed new light on the relative importance of electronic versus ionic conductivities, arguing for the need to further optimize electronic conduction in thick electrodes when they are cycled in conditions relevant to electric vehicle applications.

The energy storage performance of Li-ion batteries has continuously improved in recent years, reaching over 250 Wh/kg with an annual growth rate of 5.5 Wh/kg.[1,2] The improved performance is due to the adoption of new active materials such as nickel rich layered oxides (~200 mAh/g),[3] and the optimization of the loading amount of active materials in the electrodes by: i) reducing the thickness of electrochemically inert cell components such as current collectors, separators, and packaging and ii) diminishing the contents of the inactive components (e.g., carbon black and binder) in composite electrodes. Nevertheless, energy density improvement is still one of the most urgent issues preventing Li-ion batteries in electric vehicle applications from increasing the travel distance per charge. Because the reduction of the inactive cell and electrode components of current Li-ion batteries is physically limited to maintain safety and electrochemical performance, increasing the active material loading amount and electrode thickness is a promising option that could achieve a higher energy density in the near future.

Unfortunately, increasing the thickness of the electrode generally results in electrochemical performance deterioration. Zheng et al. reported considerable rate and cycle performance deterioration of 100 μm thick LiNi$_{1/3}$Co$_{1/3}$Mn$_{1/3}$O$_2$ electrode,[4] while Singh et al. demonstrated 63% capacity retention of 320 μm thick LiNi$_{1/3}$Co$_{1/3}$Mn$_{1/3}$O$_2$ electrode at a current density of C/2.[5] Past research, primarily based on modeling, concludes that electrochemical reactions in porous electrodes are limited by liquid-phase transport mechanisms attributed to a concentration gradient and subsequent electrolyte depletion under high current densities.[6,7] Based on the liquid-phase transport limitation theory, some groups have focused on addressing the low ionic conductivity resulting from the tortuosity of the thick electrodes to improve the electrochemical reaction at high current densities. A basic idea is to generate straight channels in composite electrode structures. Sacrificial components such as carbon black or magnetic particles have been employed to form straight channels in 220 to 310 μm thick LiCoO$_2$ electrodes, thus improving the rate performance.[8,9] Meanwhile, laser drilling has also been employed to form ionic channels in the 100 μm thick LiNi$_{1/3}$Co$_{1/3}$Mn$_{1/3}$O$_2$ electrode.[10] Freeze tape casting method is also potentially useful in

creating unidirectional columnar macropores in the thick cathode.[11] Groups have also focused on three-dimensional current collectors to reduce electronic travel distance. Wang et al. demonstrated that ultrathick electrodes (1.2 mm thick) could be cycled more than 20 times using aluminum and copper three-dimensional foam current collectors for a LiNi$_{1/3}$Co$_{1/3}$Mn$_{1/3}$O$_2$ cathode and graphite anode,[12] respectively. Abe et al. reported long-term cyclability (~2000 cycles) of a 400 μm thick LiFePO$_4$ cathode using a porous three-dimensional aluminum current collector.[13] The relationship between electronic conducting pathways attributed to inactive components in the cathode and resulting electrochemical performances was also evaluated through the optimization of carbon black/binder composite[14,15] and modification of aluminum current collector surface.[16] Since the effects of ionic and electronic conductivities in thick electrodes have not been compared at the same time in previous studies, it is necessary to understand how they affect electrochemical performance when they are simultaneously tuned in order to design an optimum thick electrode, which is the focus of the current study.

In order to evaluate the effects of electronic and ionic conductivities on electrode performance, it is necessary to fabricate electrodes with the same overall porosity and composition but with different microstructures. The mud-cracking phenomenon was used by varying the solids content, solvent and loading to create electrodes with differing microstructures, thus enabling electronic and ionic conductivities to be compared directly as a function of electrode structure. It is possible to achieve this by using techniques such as freeze drying or laser drilling. Here we choose to use mud-crack formation for two reasons: i) it provides straight ionic channels without additional manufacturing cost and ii) it is readily controlled by slurry components such as particles and solvents. Electronic conductivity of mud-cracked electrodes could also be tuned by microstructural changes based on the polymeric binder distribution[17,18] as well as the electronic pathways associated with carbon black particles.[14,19] In this work, the ionic and electronic conductivities are measured in a cathode/cathode symmetric cell with non-intercalating electrolyte salts through electrochemical impedance spectroscopy (EIS). The galvanostatic charge/discharge cycling performances of samples with a range of crack densities are then measured. The impact of this work to prove which conducting effect – electronic or ionic – is more significant will influence the direction of future research as well as the selection of materials and design parameters to benefit the more critical conductivity element.

*Electrochemical Society Student Member.
**Electrochemical Society Member.
zE-mail: piliu@eng.ucsd.edu

Experimental

Materials and slurry preparation.—Commercial LiNi$_{0.8}$Co$_{0.1}$Mn$_{0.1}$O$_2$ particles (NCM 811, Ecopro) was used as cathode material, and carbon black (Super C65, Timcal) and Poly(vinylidene fluoride-hexafluoropropylene) (PVDF-HFP, Kynar Flex 2801) were used as conducting agent and binder. Binder solution with 10 wt% concentration was prepared by dissolving PVDF-HFP in *N*-Methyl-2-pyrrolidone (NMP, Sigma Aldrich). NCM 811 and carbon black in an 80:10 by weight ratio were premixed using agate mortar and pestle for 15 min. Then, the binder solution and additional NMP were added to the powder mixture to prepare the cathode slurries in an 80:10:10 weight ratio of NCM 811 : carbon black : PVDF-HFP. The slurries were ball-milled overnight with ZrO$_2$ balls with a 1:1 ball-to-powder weight ratio.

The solids content in the slurries and solvent species served as the crack density controlling parameters. The solids content in the slurries were carefully controlled from 27 to 35 wt% based on NMP solvent, while the NMP, *N,N*-Dimethylformamide (DMF, Sigma Aldrich), and NMP-Acetone mixtures were chosen as the solvents for slurries to influence the volatility and investigate the solvent species effect.

Crack morphology characterization.—The morphology and crack densities were quantitatively characterized using scanning electron microscopy (SEM, FEI). The total crack length per unit area was carefully measured in order to quantify the crack density. Note that the initial crack width (before calendaring) was not considered since the crack becomes narrower to less than a few μm regardless of the initial width.

Electrode preparation.—The slurries were cast on aluminum foil, and the active material loading was controlled at around 25 mg/cm^2. By comparison, the loading of commercial product is around 10 mg/cm^2.[20] The cast electrodes were dried at 60°C overnight to remove the solvents, and subsequently heated at 200°C for 30 min to prevent delamination. The electrodes were then cut into disks with a diameter of 15 mm, and subsequently calendared to a porosity of 30% by roll-pressing. Calculation of porosity is based on the true density calculation using the following equation.[20]

$$\varepsilon = \frac{V_{electrode} - \sum V_{component}}{V_{electrode}}$$

$$= \frac{V_{electrode} - M_{electrode} \cdot \left(\frac{P_{AM}}{\rho_{AM}} + \frac{P_{CB}}{\rho_{CB}} + \frac{P_{binder}}{\rho_{binder}} \right)}{V_{electrode}}$$

where ε is the porosity of electrode, V$_{electrode}$ and V$_{component}$ are the electrode and components volume (e.g., active materials, carbon black, and binder), M$_{electrode}$ is the mass of the cathode disk, and P and ρ are the mass fraction and density of the materials. The densities of the active material, carbon black and binder used for porosity calculation were 4.7, 2.0, and 1.78 g/cm^3, respectively. The cathodes for galvanostatic charge/discharge test were further prepared by cutting disks of a 12 mm diameter.

Electrochemical impedance spectroscopy measurements.—Two cathode disks with a 15 mm diameter were symmetrically assembled into the 2032-type coin-cell in order to measure the ionic conductivity using AC impedance on the basis of the transmission-line model.[21] Non-lithium electrolyte (0.1 M tetrabutylammonium perchlorate (TBAClO$_4$, Sigma Aldrich, ≥99.0%) in ethylene carbonate (EC, BASF) : dimethyl carbonate (DMC, BASF) (1:1 w/w)) was employed for ideal polarization by preventing charge transfer reactions.[22] The symmetric cathodes were assembled in the 2032-type coin-cell (See Figure S1). The electrochemical impedance spectra (EIS) was measured around open circuit voltage in a range from 1 MHz to 100 mHz with a perturbation amplitude of 10 mV.

Galvanostatic charge/discharge cycling for rate and cycling performance.—The cathode performance was evaluated by assem-

bling the 12 mm diameter disk in 2032 type coin-cells. Li metal was used as a counter electrode with a Celgard separator. 1 M LiPF$_6$ (BASF) electrolyte was synthesized in ethylene carbonate (EC, BASF) : ethyl methyl carbonate (EMC, BASF) (3:7 w/w) with 2 wt% vinylene carbonate (VC, BASF). Two formation cycles at C/10 charge and discharge without rest were conducted at a 2.8 to 4.4 V range. Rate performance was assessed by charging with constant current at C/3 (until 4.4 V) and subsequent constant voltage at 4.4 V (until the current is below C/20) and then discharging with constant current at various current densities (e.g., C/5, C/3, C/2, 1C, 2C and C/5) until 2.8 V. The cycling performance was also characterized after the rate test by CC-CV charging and CC discharging between 2.8 and 4.4 V at C/3.

Results and Discussion

Crack densities of mud-cracked electrodes.—The principle of the mud-crack formation is that the induced stress driven by solvent evaporation exceeds the material strength of the cathode and subsequent cracks rupture through the thickness during the drying process.[23,24] Figure 1a shows how mud-cracks form straight channels all the way through to the current collector. In a normal cell, the distribution of Li ions and electrons is assumed to be relatively homogenous across the surface of the electrode, leading to an even depth of discharge gradient (Figure 1b). Introduction of ionic channels facilitates the ion supply to the bottom of electrode, but locally deteriorates interfacial electronic contact by delamination,[25] leading to a less electrochemically active region due to retarded electron supply and resulting in an affected discharge profile (Figure 1c). Calendaring of the electrode after crack formation will reduce the width of the channel and improve the interfacial contact, but the physical picture illustrated in Figure 1c should remain.

Figure 2a reveals that the mud-cracked electrodes were readily prepared by employing a high concentration of the C65 carbon black and PVDF-HFP binder (10 wt% each) where the loadings of the active material were around 25 mg/cm^2. NMP was used as a solvent, and the solids content in the slurry was 35 wt%. The initial crack widths before calendaring are on the scale of tens of microns and the mud-cracks form straight channels as shown in Figure 2b. The top-view and cross-sectional SEM images of the calendared electrodes in Figure 2c and (d) demonstrate that the channels remain as hairline cracks. Channels are expected to act as ionic highways. The limited total porosity of the electrode requires that areas of greater ionic channel gaps be balanced by areas of higher density, therefore, a narrower gap is preferable in order to prevent the inferior ionic conductivity driven by high tortuosity in the cathode matrix.[8]

Based on the successful mud-crack formation, various slurry compositions are examined to control the crack density and interfacial electronic contact between the cathode coating layer and the aluminum current collector. The electrode composition and loading are carefully maintained to evaluate the structural effect on the electrochemical performances. The slurry compositions (e.g., solids content in the slurry and solvent composition) are selected as parameters for controlling the cathode microstructure. Here, the crack density is defined as total crack length per unit area (μm/mm^2) before calendaring. The initial crack width is not considered since the gap between grains remains as a hairline crack after calendaring as discussed above.

First, the solids content concentration in NMP based slurries is varied from 27 to 33 wt% as summarized in Figure 3a. The lower solids content concentration was expected to have a lower crack density due to the longer drying time and subsequent lighter stress evolution. Indeed, the crack density at 27 wt% of 1939.8 (± 303.6) μm/mm^2 is significantly lower than those of 30 and 33 wt% (2081.7 (± 230.5) and 2124.2 (± 196.0) μm/mm^2, respectively. Although the standard deviations of crack densities are larger than the differences between the crack densities of the sample groups, the data is statistically meaningful since each data point was collected from ten SEM images with an area of 4.584 mm^2, and the areas of the electrodes for the electrochemical performance (e.g., 113.1 mm^2 (12 mm disk for galvanostatic
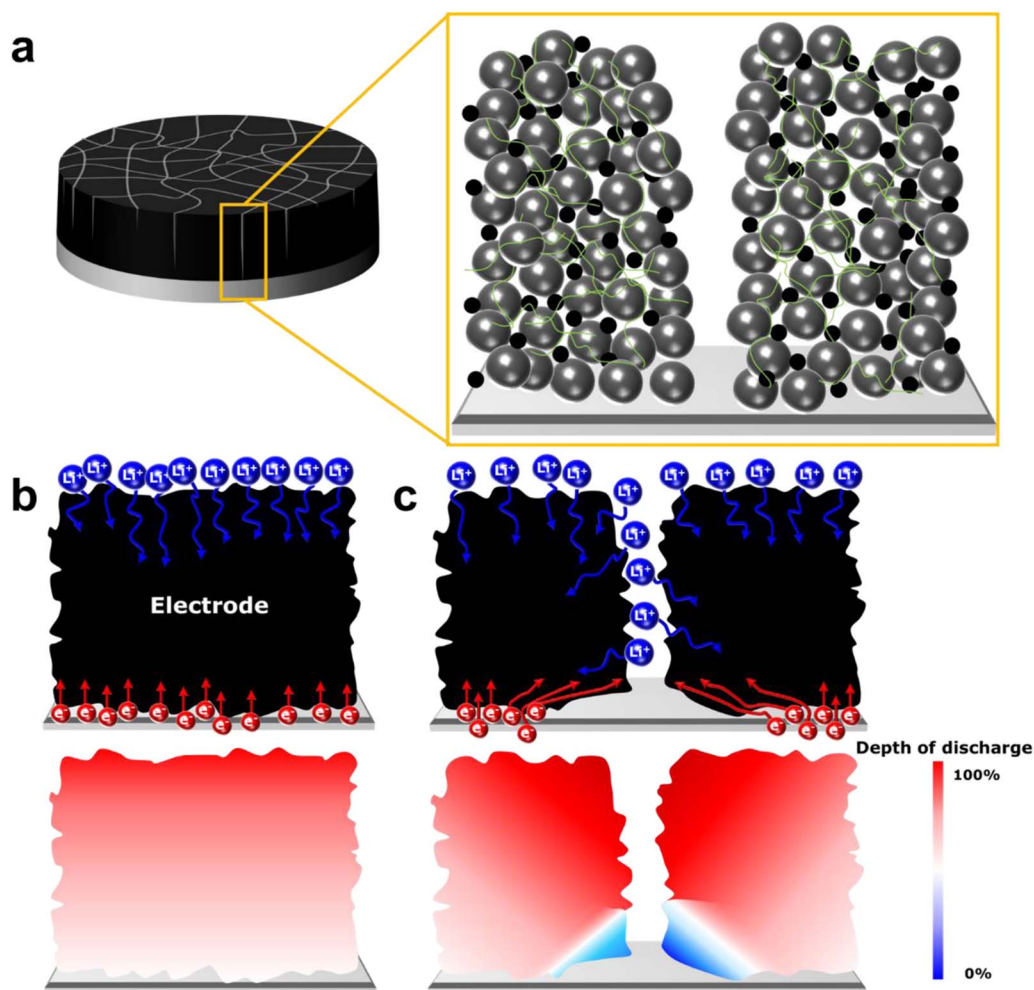
Figure 1. Schematic diagrams of mud-crack formed electrode (a) and comparison of general and mud-cracked discharge process and expected depth of discharge profiles in a normal electrode (b) and mud-cracked electrode (c).
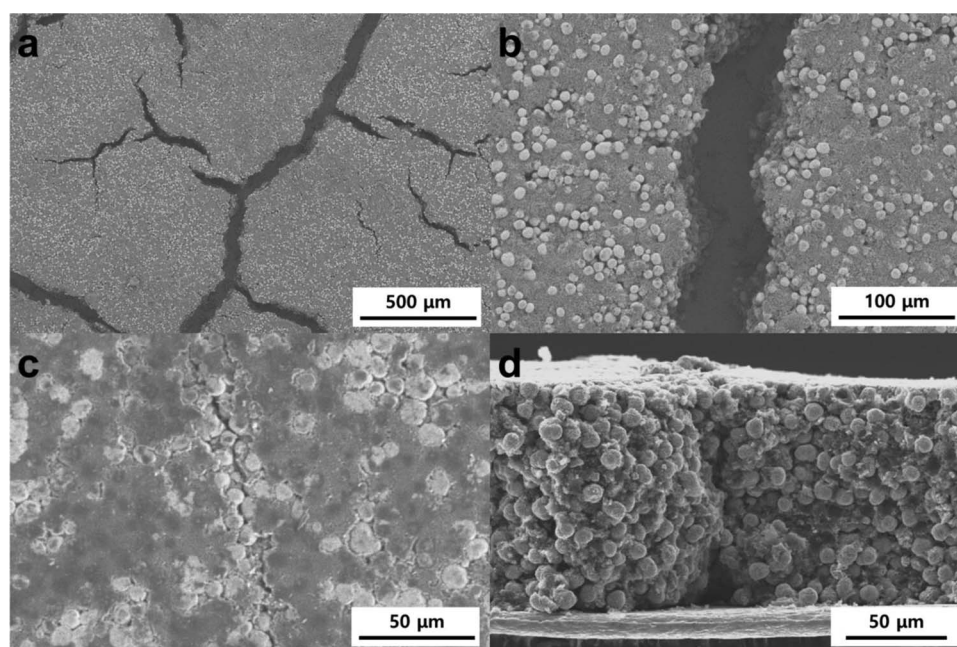

Figure 2. SEM images of electrodes: top-view of as-dried electrodes with (a) low and (b) high magnifications, and (c) top-view and (d) cross-section of the pressed electrodes.
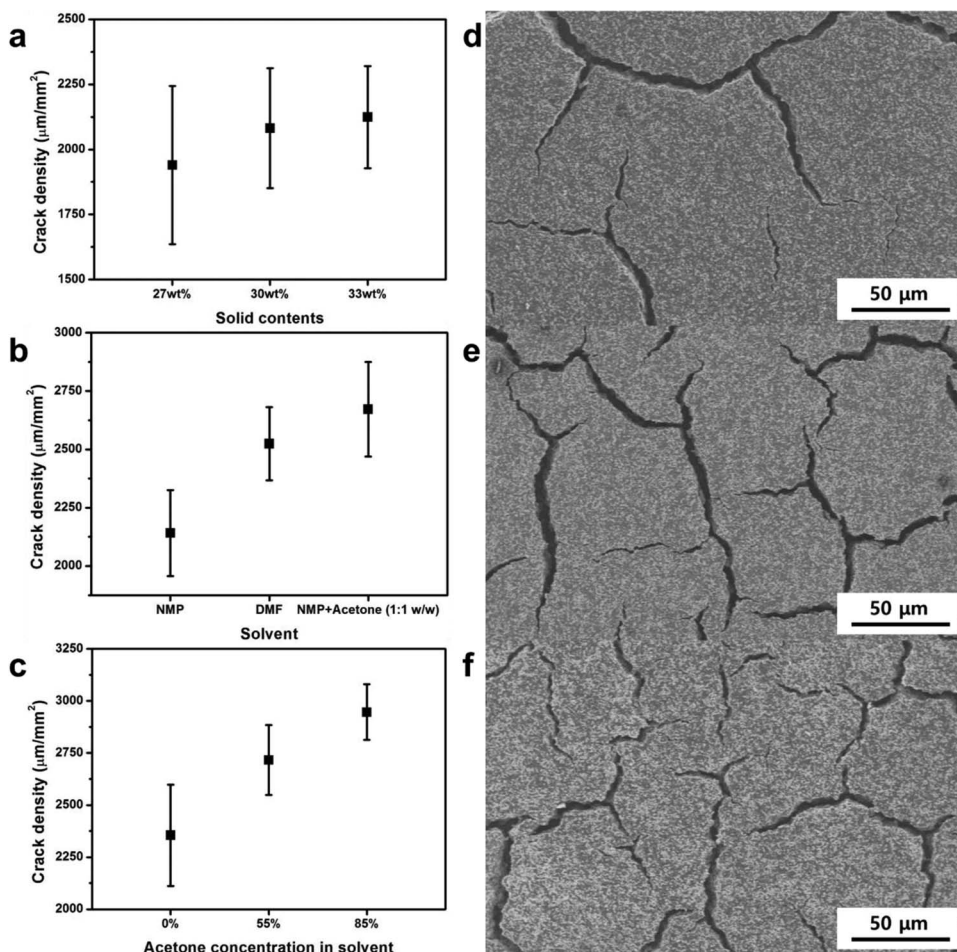
Figure 3. Crack density control by the slurry parameters: (a) solids content in NMP-based slurry, (b) various solvent, and (c) acetone concentration in acetone/NMP solvent mixture, and representative SEM images of (d) solid content of 27 wt% in (a), (e) DMF solvent in (b), and (f) acetone 85% in (c).

charge/discharge cycling tests) and 176.7 mm² (15 mm disk for symmetric EIS tests)) are much larger than the measured area.

At the same time, more volatile solvents such as DMF (T_b = 153°C) and acetone (T_b = 56°C) were used to achieve greater changes in crack densities. The solids content of the slurries was thoroughly controlled at 35 wt%. The DMF based slurry results in the increased crack density of 2524.0 ($\pm$ 157.1) μm/mm² compared to the NMP based slurry of 2141.6 ($\pm$ 184.2) μm/mm². Meanwhile, the NMP and acetone mixture was used instead of the pure acetone based slurry because the acetone based slurry totally delaminated from the current collector during drying process (refer to Figure S2). The 1:1 NMP/acetone ratio sample shows an average crack density of 2672.3 ($\pm$ 203.1) μm/mm², and the crack density changes are summarized in Figure 3b. As shown in Figure 3c, changing the NMP/acetone ratio from 100 to 15 wt% leads to an increase in crack density to 2716.4 ($\pm$ 168.2) and 2946.1 ($\pm$ 133.7) μm/mm² at 45 and 15 wt% NMP concentration in solvent mixture. Overall, crack density increases with an increase in solids content and acetone concentration. The increase in solvent volatility decreases the amount of time required for drying and thus affects the kinetics of drying which determine the crack structure. Qualitatively, unit cracks shorten and curve more as the crack density increases (refer to Figures 3d-3f).

Electrochemical impedance spectroscopy (EIS) of symmetric cell.—Electrochemical impedance spectroscopy (EIS) is a well-known electrochemical characterization method which can provide insight on the electrochemical systems such as Li-ion diffusion in electrolyte, solid electrolyte interphase (SEI) formation, and charge transfer reactions, etc.[26] The transmission line model (TLM) for cylin-

drical pores can be combined with EIS using symmetric cells to analyze internal resistance of electrodes.[21,27] Symmetric cells were prepared to evaluate the precise internal resistance of their specific electrodes without the influence of the counter electrode. Meanwhile, a non-intercalating salt (TBAClO₄) eliminates the charge transfer reaction effect which depends on the active material composition.[22] The EIS of the symmetric cell based on a non-intercalating salt allows for evaluation of the inherent electrode architecture and interfacial properties between current collector and electrode layer.

EIS curves of the mud-cracked electrodes with various crack densities ranging from $1940 - 2946$ μm/mm² in Figure 4 reveal the typical Nyquist plot of the cathode symmetric cell consisting of three components: i) a semi-circle from high to mid frequency (e.g., 30 kHz to 400 Hz), ii) a 45° slope from mid to low frequency (e.g., 400 to 2 Hz), and iii) a steep slope at low frequency (e.g., <2 Hz). High frequency intercept of the semi-circle at around 30 kHz is related to the electrolyte bulk resistance, and the resistance of the semi-circle at high frequency impedance (>400 Hz) corresponds to the contact resistance at the aluminum current collector/cathode layer interface.[22,28,29] The 45° slope at intermediate frequency represents the mobility of ions inside the porous electrode.[27] The steep slope at low frequency (<2 Hz) corresponds to the capacitive behavior of electrical double layer and the pore geometry and side reactions cause the non-uniform current distribution, reflected as the non-vertical line.[27] The ionic resistance corresponds to geometric parameters and should therefore be geometrically normalized for fair comparison. However, because the contact resistance is an interfacial property and the tested electrode area is fixed as 1.767 cm², the contact resistance was directly compared without further normalization. The effective ionic conductivity
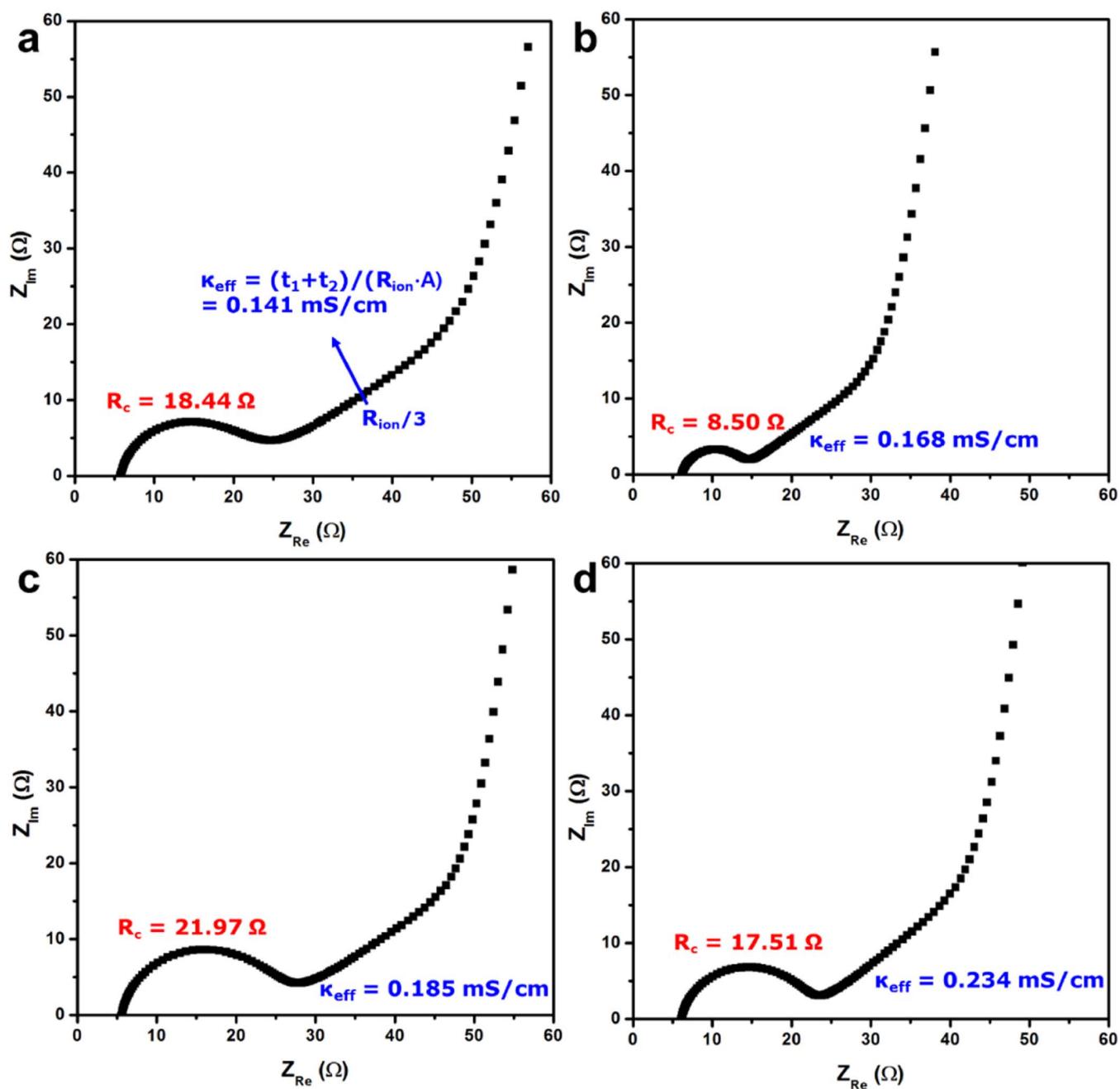
Figure 4. Exemplary EIS curves of symmetric cells with crack density of (a) 1940, (b) 2355, (c) 2716, and (d) 2946 μm/mm^2.

(κ_{eff}) is calculated from the 45° slope in Figure 4 and normalized by thickness to ensure that any slight variation during fabrication is accounted for. Figure 5 reveals the effective ionic conductivity and electronic contact resistance with various crack densities including the measurement shown in Figure 4. The ionic conductivity increases from 0.141 to 0.234 mS/cm as the crack density increases, while the contact resistance (R_c) does not follow the crack density trend as directly. The trends of interfacial contact resistance in the top graph of Figure 5 show: i) reduced R_c with an increase in solids content in NMP mono-solvent, and ii) increased R_c with a mixed or more volatile solvent system. The second trend is further supported by galvanostatic charge/discharge curves discussed in the following section. On the other hand, the effective ionic conductivity is increased as the crack density increases (refer to the bottom graph in Figure 5). Four groups of samples with the highest and lowest values of κ_{eff} and R_c were se-

lected from the top graph to examine the effect of ionic conductivity on the electrochemical performances as depicted.

Galvanostatic charge/discharge cycling test for rate and cycling performance evaluation.—The rate and cycling performances of the selected samples were examined using a galvanostatic charge/discharge cycling test. The initial coulombic efficiencies of samples 1–4 are 72.16% ($\pm$ 0.18%), 76.07% ($\pm$ 1.31%), 71.61% ($\pm$ 0.50%), and 71.52% ($\pm$ 1.25%), while the first discharge capacities at C/10 are 166.78 ($\pm$ 0.72), 178.29 ($\pm$ 4.14), 166.30 ($\pm$ 2.17), and 170.23 ($\pm$ 3.25) mAh g^{-1}, respectively (Table I). The current densities are calculated based on the expected capacity of 1C = 210 mAh g^{-1}. Both the initial coulombic efficiency and first discharge capacity of sample 2 with the lowest R_c value at symmetric cell EIS test results are significantly higher than those of the other groups.
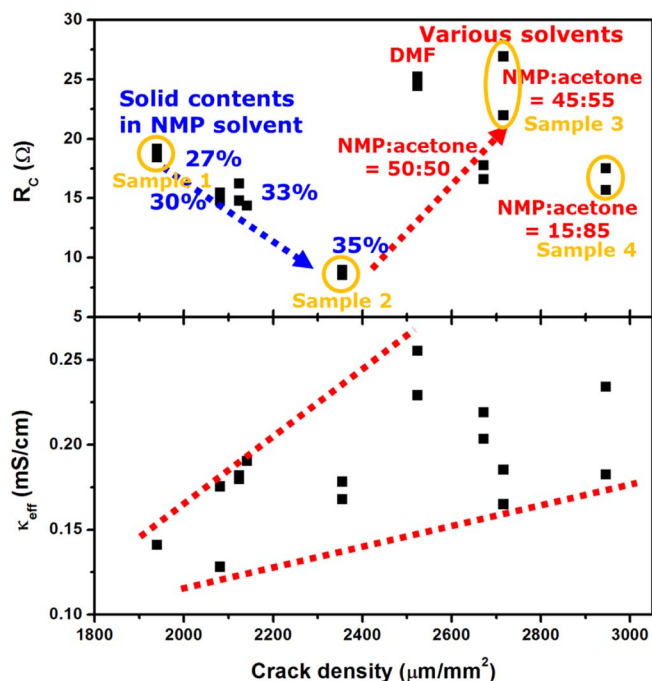
Figure 5. Summary of symmetric two cathode EIS characterization in TBAClO$_4$ electrolyte: contact resistance (R$_c$) between cathode layer and Al current collector and effective ionic conductivity (κ_{eff}) calculated from ionic resistance (R$_{Ion}$).

The discharge profiles in Figures 6a-6d reveal that the decrease of onset reduction potential, due to the internal resistance (IR) drop, of the discharge profiles intensifies as the current density increases, and the IR drop is highly related to the R$_c$. Despite the considerable IR drops, the mud-cracked electrodes, at C/5 and C/3, still deliver specific capacities of more than 94% of the initial discharge capacity at C/10. The two typical reduction peaks related to Co^{3+}/Co^{4+} and Ni^{2+}/Ni^{4+} redox pairs[30] develop distinctly at around 4.2 and 3.7 V at a low current density of C/10 as shown by the dQ/dV∼V curves in Figures 6e-6h. Note that the tetravalent stated Mn stabilizes the high-delithiated local structure rather than providing capacity.[31] Although the peak at around 4.2 V significantly shifted to lower potential ($\triangle$V$_{C/10\ to\ C/3}$ = 0.07–0.19 V) as the current density increased, the peak intensity gradually increased (refer to Figure S3). Meanwhile, the peak potential at around 3.7 V shifted less ($\triangle$V$_{C/10\ to\ C/3}$ = 0.04–0.06 V), and the peak intensity decreased due to the increased current density.

On the other hand, the electrochemical performances at high current densities ($\geq$ C/2) are significantly degraded as the electronic conductivity is reduced. The discharge capacities of all the samples are normalized with respect to their initial discharge capacity during the first cycle of C/10. The average normalized discharge capacities of sample 2 (featuring the lowest R$_c$) at the current densities of C/2, 1C, and 2C are 94.35%, 78.74%, and 17.69%, while those of sample 3 (highest R$_c$) are 86.97%, 49.82%, and 8.22%, respectively (refer to

Figure 7a). Although the effective ionic conductivity of sample 4 is much higher than that of sample 1, its rate performances are not distinguishable: the average normalized discharge capacities of sample 1 at C/2, 1C, and 2C are 93.78%, 67.73%, and 7.87%, while those of sample 4 are 92.14%, 60.71%, and 7.71%. The depressed discharge reactions at high current densities are caused by the discharge reaction happening preferentially at particles with lower inter-particle resistance.[32] The discharge capacities of all samples are fully recovered at a current density of C/5 at the 28th and subsequent cycles.

The cycling performances were continuously evaluated following the rate performances test. The average values of the normalized discharge capacities of the four sample groups in Figure 7b reveal the same trend as the rate performance. The number of cycles for which the average cycling retention of each sample is 80% or less are 83 (sample 1), 91 (sample 2), 75 (sample 3), and 81 (sample 4). The improved cycling performance in sample 2 is attributed to the improved electronic conducting network compared to other groups.[33] The cycling degradation behaviors of the cathodes are shown in voltage profiles and differential discharge capacity curves in Figure S4. The electrochemical reactions at high potential peaks (e.g., 4.0–4.2 V) are considerably suppressed as the cycle number increases. Dramatic degradation of NMC 811 electrodes may be due to the overlapped potentials of the Co^{3+}/Co^{4+} redox and O$_2$ evolution onset by electrolyte oxidation at the cathode surface[34–36] as well as mechanical failure such as micro cracks by repetitive volume change during cycling.[37–39] In brief, it can be concluded that the electrochemical performances of the cracked electrodes are more closely related to the interfacial resistance than the ionic conductivity tuned by the crack densities.

Further examination of interfacial contact effect.—In order to further quantify the electronic conducting effect at the interface, a simple experiment was conducted to compare cathodes with different current collector metals. Free-standing cathodes with gold current collector were prepared by peeling off the aluminum current collector and sputtering gold on those cathode surfaces as shown in Figure S5 (a). The details on the sample preparation and rate performance test are described in Supplementary Information. The loadings of the gold sputtered electrodes and the reference group with the aluminum current collector were controlled at around 60 mg/cm^2. The rate performances of these electrodes at C/3 and C/2 rates are highly deteriorated compared to the initial cracked electrodes due to the higher loading and the lower amount of carbon black content. However, the sputtered gold current collector provides far higher normalized discharge capacities at those current densities (68.66% and 38.00%) in comparison to the aluminum current collector electrodes (38.88% and 12.94%) because of reduced contact resistance (refer to Figure S5 (b)). The pronounced difference between discharge capacities of gold versus aluminum current collector cathodes illustrates the importance of addressing interfacial electronic resistance at high loadings and moderate C rates. This work assumes the electronic conducting nature between the active material particles and binder components to be analogous to that of the current collector and active material particle interface because both the aluminum current collector and NMC particles have the oxide layer at their surface.[40] Future research can further quantify the carbon black and binder distribution and how they interact with the oxide particles.

Table I. Summary of electrochemical performance data of sample groups 1–4 showing that electronic resistance is a greater indicator of performance than ionic conductivity under certain conditions.

| Sample	Composition	Conductivity	Coulombic Efficiency	Discharge Capacity (mAh g^{-1})	Average Normalized Discharge Capacity (%)			No. of cycles at 80% Capacity
				C/10	C/2	1C	2C	
1	NMP with 27% solids content	Low κ_{eff}	72.16%	166.78	93.78	67.73	7.87	83
2	NMP with 35% solids content	Low R$_c$	76.07%	178.29	94.35	78.74	17.69	91
3	NMP : acetone = 45:55	High R$_c$	71.61%	166.30	86.97	49.82	8.22	75
4	NMP : acetone = 15:85	High κ_{eff}	71.52%	170.23	92.14	60.71	7.71	81
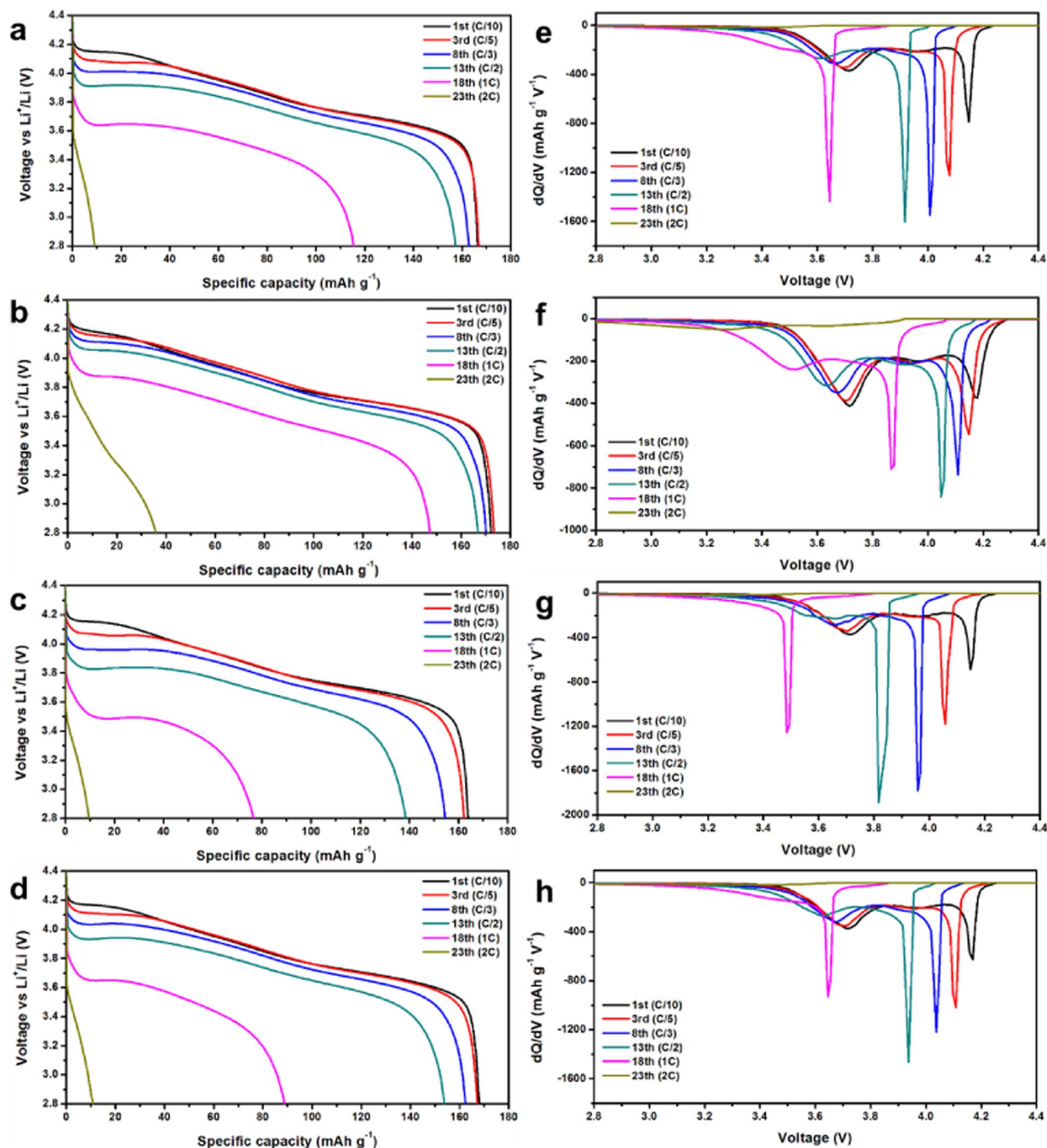
Figure 6. Voltage profiles (a-d) and differential capacity curves (e-h) of the cracked electrode discharge with various current densities: (a and e) Sample 1, (b and f) Sample 2, (c and g) Sample 3, and (d and h) Sample 4.

Conclusions

Mud-crack formation was employed to create high loading, low tortuosity electrodes. Various crack density samples were prepared by controlling the slurry compositions. The ionic conductivity increases with the crack density due to the formation of more straight, vertical ionic channels, while the electronic conductivity is also affected due to the varying carbon black and binder distribution. This mechanism

thus allows the fabrication of electrodes with the same compositions and porosities but with different microstructure which result in varied electronic and ionic resistances. Four groups of samples with the highest and lowest values of κ_{eff} and R_c were chosen to illustrate the effects of the ionic and electronic conductivity on the electrochemical performances. Although the low rate cycling performances are excellent regardless of the ionic and electronic conductivity, the galvanostatic charge/discharge behaviors at high rates ($\geq$ C/2) and
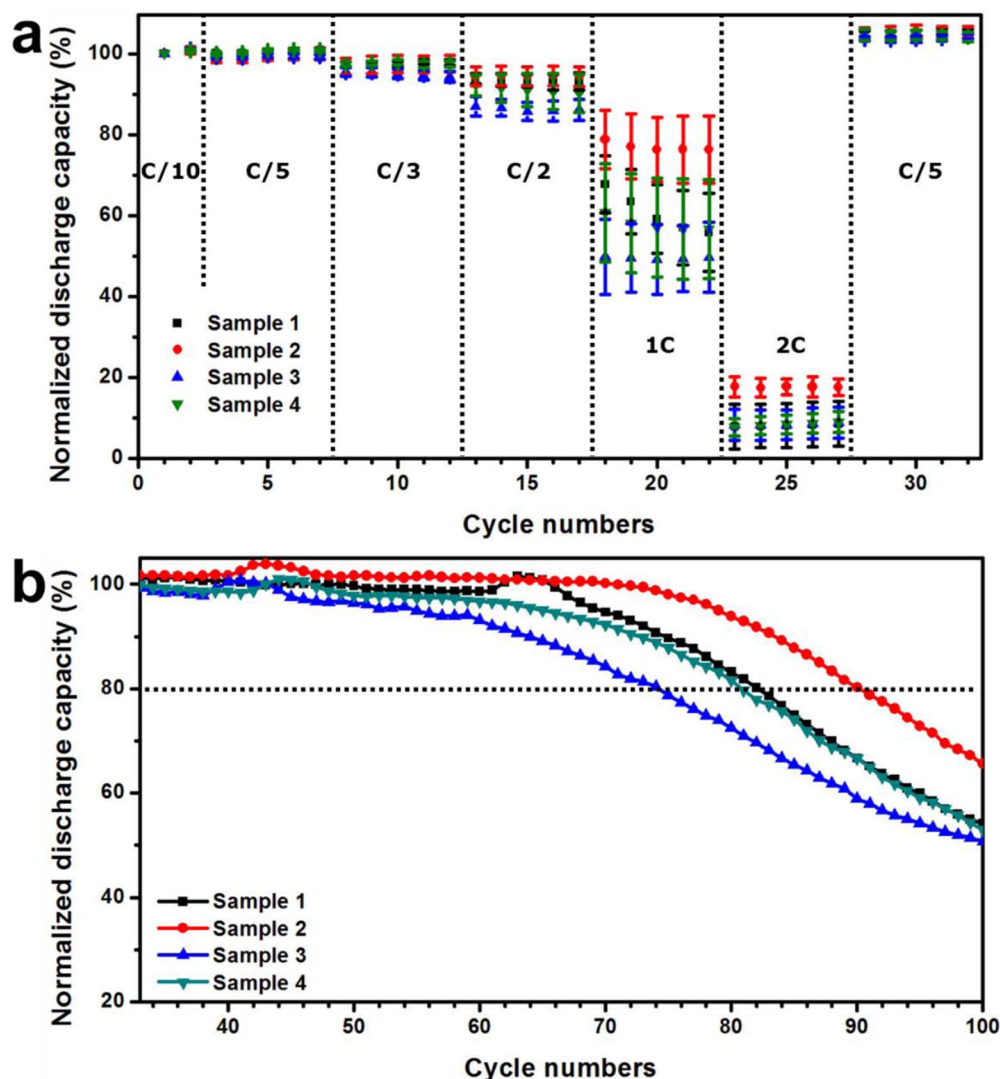
Figure 7. Average normalized discharge capacities of the cracked samples: (a) rate performances discharged at different current densities and (b) cycling performances cycled at C/3.

the cycling performances at a rate of C/3 are more closely related to the electronic conductivity than the ionic conductivity. Experiments comparing electronic interfacial contact resistance of gold-sputtered and aluminum current collectors further support the conclusion that electronic conductivity plays a greater role in electrochemical performance than ionic conductivity for thick electrodes fabricated in this study.

ORCID

Ping Liu https://orcid.org/0000-0002-1488-1668

References

1. H. Sasaki, T. Suzuki, M. Matsuu, Y. Kono, H. Takahashi, R. Yanagisawa, K. Watanabe, A. Fujisawa, Y. Yamamoto, K. Takeda, M. Matsumura, S. Hirakawa, C. Amemiya, N. Hamanaka, and N. Oda, *iMLB 2016 Meeting Abstracts*, **MA2016-03**, 99 (2016).

2. C.-X. Zu and H. Li, *Energy Environ. Sci.*, **4**, 2614 (2011).
3. N. Nitta, F. Wu, J. T. Lee, and G. Yushin, *Mater. Today*, **18**, 252 (2015).
4. H. Zheng, J. Li, X. Song, G. Liu, and V. S. Battaglia, *Electrochim. Acta*, **71**, 258 (2012).
5. M. Singh, J. Kaiser, and H. Hahn, *J. Electrochem. Soc.*, **162**, A1196 (2015).
6. H. Hafezi and J. Newman, *J. Electrochem. Soc.*, **147**, 3036 (2000).
7. V. Srinivasan and J. Newman, *J. Electrochem. Soc.*, **151**, A1517 (2004).
8. C.-J. Bae, C. K. Erdonmez, J. W. Halloran, and Y.-M. Chiang, *Adv. Mater.*, **25**, 1254 (2013).
9. J. S. Sander, R. M. Erb, L. Li, A. Gurijala, and Y. M. Chiang, *Nat. Energy*, **1**, 16099 (2016).
10. P. Smyrek, J. Pröll, H. J. Seifert, and W. Pfleging, *J. Electrochem. Soc.*, **163**, A19 (2016).
11. M. A. Ghadkolai, S. Creager, J. Nanda, and R. K. Bordia, *J. Electrochem. Soc.*, **164**, A2603 (2017).
12. J. S. Wang, P. Liu, E. Sherman, M. Verbrugge, and H. Tataria, *J. Power Sources*, **196**, 8714 (2011).
13. H. Abe, M. Kubota, M. Nemoto, Y. Masuda, Y. Tanaka, H. Munakata, and K. Kanamura, *J. Power Sources*, **334**, 78 (2016).
14. G. Liu, H. Zheng, A. S. Simens, A. M. Minor, X. Song, and V. S. Battaglia, *J. Electrochem. Soc.*, **154**, A1129 (2007).
15. G. Liu, H. Zheng, X. Song, and V. S. Battaglia, *J. Electrochem. Soc.*, **159**, A214 (2012).
16. H.-C. Wu, H.-C. Wu, E. Lee, and N.-L. Wu, *Electrochem. Commun.*, **12**, 488 (2010).
17. M. Yoo, C. W. Frank, S. Mori, and S. Yamaguchi, *Chem. Mater.*, **16**, 1945 (2004).
18. R. Gregorio and D. S. Borges, *Polymer*, **49**, 4009 (2008).
19. R. Dominko, M. Gaberšček, J. Drofenik, M. Bele, and J. Jamnik, *Electrochim. Acta*, **48**, 3709 (2003).

20. H. Zheng, L. Tan, G. Liu, X. Song, and V. S. Battaglia, *J. Power Sources*, **208**, 52 (2012).
21. N. Ogihara, Y. Itou, T. Sasaki, and Y. Takeuchi, *J. Phys. Chem. C*, **119**, 4612 (2015).
22. J. Landesfeind, J. Hattendorff, A. Ehrl, W. A. Wall, and H. A. Gasteiger, *J. Electrochem. Soc.*, **163**, A1373 (2016).
23. V. Lazarus and L. Pauchard, *Soft Matter*, **7**, 2552 (2011).
24. R. Weinberger, *J. Struct. Geol.*, **21**, 379 (1999).
25. J. Zhang, Y. Lu, L. He, L. Yang, and Y. Ni, *Eng. Fract. Mech.*, **177**, 123 (2017).
26. H. Zheng, G. Liu, X. Song, P. Ridgway, S. Xun, and V. S. Battaglia, *J. Electrochem. Soc.*, **157**, A1060 (2010).
27. N. Ogihara, S. Kawauchi, C. Okuda, Y. Itou, Y. Takeuchi, and Y. Ukyo, *J. Electrochem. Soc.*, **159**, A1034 (2012).
28. M. Gaberscek, J. Moskon, B. Erjavec, R. Dominko, and J. Jamnik, *Electrochem. Solid State Lett.*, **11**, A170 (2008).
29. C. Portet, P. L. Taberna, P. Simon, and C. Laberty-Robert, *Electrochim. Acta*, **49**, 905 (2004).
30. F. Wu, J. Tian, Y. Su, J. Wang, C. Zhang, L. Bao, T. He, J. Li, and S. Chen, *ACS Appl. Mater. Interfaces*, **7**, 7702 (2015).
31. A. Manthiram, B. Song, and W. Li, *Energy Storage Mater.*, **6**, 125 (2017).
32. I. V. Thorat, T. Joshi, K. Zaghib, J. N. Harb, and D. R. Wheeler, *J. Electrochem. Soc.*, **158**, A1185 (2011).
33. X. Li, X. Zhao, M.-S. Wang, K.-J. Zhang, Y. Huang, M.-Z. Qu, Z.-L. Yu, D.-S. Geng, W.-G. Zhao, and J.-M. Zheng, *RSC Adv.*, **7**, 24359 (2017).
34. R. Jung, M. Metzger, F. Maglia, C. Stinner, and H. A. Gasteiger, *J. Electrochem. Soc.*, **164**, A1361 (2017).
35. J. Li, L. E. Downie, L. Ma, W. Qiu, and J. R. Dahn, *J. Electrochem. Soc.*, **162**, A1401 (2015).
36. L. Li, Z. Chen, Q. Zhang, M. Xu, X. Zhou, H. Zhu, and K. Zhang, *J. Mater. Chem. A*, **3**, 894 (2015).
37. H.-J. Noh, S. Youn, C. S. Yoon, and Y.-K. Sun, *J. Power Sources*, **233**, 121 (2013).
38. A. O. Kondrakov, A. Schmidt, J. Xu, H. Geßwein, R. Mönig, P. Hartmann, H. Sommer, T. Brezesinski, and J. Janek, *J. Phys. Chem. C*, **121**, 3286 (2017).
39. J.-M. Lim, T. Hwang, D. Kim, M.-S. Park, K. Cho, and M. Cho, *Sci. Rep.*, **7**, 39669 (2017).
40. H.-C. Wu, Y.-P. Lin, E. Lee, W.-T. Lin, J.-K. Hu, H.-C. Chen, and N.-L. Wu, *Mater. Chem. Phys.*, **117**, 294 (2009).